Journal of Geophysical Research: Space Physics

RESEARCH ARTICLE
10.1029/2017JA025112

Cassini RPWS Dust Observation Near the Janus/Epimetheus Orbit

S.-Y. Ye[1], W. S. Kurth[1], G. B. Hospodarsky[1], A. M. Persoon[1], D. A. Gurnett[1], M. Morooka[2], J.-E. Wahlund[2], H.-W. Hsu[3], M. Seiß[4], and R. Srama[5]

[1]Department of Physics and Astronomy, University of Iowa, Iowa City, IA, USA, [2]IRF-U, Uppsala, Sweden, [3]LASP, University of Colorado Boulder, Boulder, CO, USA, [4]Institute of Physics and Astronomy, University of Potsdam, Potsdam, Germany, [5]Institute of Space Systems, University of Stuttgart, Stuttgart, Germany

Key Points:
- Dust particles have been detected near the Janus/Epimetheus orbit by Cassini RPWS and CDA
- From the RPWS measurements, dust density and size distribution can be derived, which is mostly consistent with CDA results
- RPWS data indicated that the dusty ring is slightly tilted and slowly precesses as it rotates around Saturn

Correspondence to:
S.-Y. Ye,
shengyi-ye@uiowa.edu

Citation:
Ye, S.-Y., Kurth, W. S., Hospodarsky, G. B., Persoon, A. M., Gurnett, D. A., Morooka, M., et al. (2018). Cassini RPWS dust observation near the Janus/Epimetheus orbit. *Journal of Geophysical Research: Space Physics*, *123*, 4952–4960. https://doi.org/10.1029/2017JA025112

Received 8 DEC 2017
Accepted 24 MAY 2018
Accepted article online 4 JUN 2018
Published online 28 JUN 2018

Abstract During the Ring Grazing orbits near the end of Cassini mission, the spacecraft crossed the equatorial plane near the orbit of Janus/Epimetheus (~2.5 *Rs*). This region is populated with dust particles that can be detected by the Radio and Plasma Wave Science (RPWS) instrument via an electric field antenna signal. Analysis of the voltage waveforms recorded on the RPWS antennas provides estimations of the density and size distribution of the dust particles. Measured RPWS profiles, fitted with Lorentzian functions, are shown to be mostly consistent with the Cosmic Dust Analyzer, the dedicated dust instrument on board Cassini. The thickness of the dusty ring varies between 600 and 1,000 km. The peak location shifts north and south within 100 km of the ring plane, likely a function of the precession phase of Janus orbit.

1. Introduction

Besides the spectacular main rings, Saturn also has a number of diffuse rings that are composed of particles nanometer to tens of micrometers in size (de Pater et al., 2004; Hamilton et al., 2015; Hedman et al., 2007; Horányi et al., 2008, 2009; Kempf et al., 2008; Spahn, Albers, et al., 2006; Spahn, Schmidt, et al., 2006; Showalter & Cuzzi, 1993; Showalter, 1996; Throop & Esposito, 1998). The small size of these particles makes them sensitive to not only the force of gravity but also nongravitational forces like solar radiation pressure and electromagnetic forces, so the dynamics of diffuse rings are drastically different from that of the main rings (Burns et al., 2001; Horányi, 1996; Tiscareno, 2013). The dynamic orbit evolution and plasma sputtering lead to short life spans of these particles, requiring dust production mechanisms to replenish the diffuse rings. While cryovolcanic activity near the south pole of Enceladus has been discovered by Cassini to be the source of E ring material (Porco et al., 2006; Spahn, Albers, et al., 2006; Waite et al., 2006), other diffuse rings are formed through collisions (meteoroid-moonlet impacts or collisions among the small bodies) and diffusion of collisional debris by nongravitational forces (Hedman et al., 2007; Williams & Murray, 2011).

Saturn's faint rings offer the special opportunity to be studied by both remote sensing and in situ observations. The remote sensing of the faint rings of Saturn started from ground-based observations during equinox, when line-of-sight optical depths of the faint rings are greatly enhanced and the glare from the main rings is minimal (de Pater et al., 2004; Nicholson et al., 1996). Remote sensing of the faint rings of Saturn by the Voyagers and Cassini revealed 3-D structures and put constraints on the size distribution of the ring particles (Hedman et al., 2007, 2012; Showalter, 1996; Showalter et al., 1991). Dust impacts on the spacecraft induced signals in the Plasma Wave Science and Planetary Radio Astronomy instruments onboard Voyager 2 during its Saturn flyby, providing the first in situ observations of Saturn's faint rings (Aubier et al., 1983; Gurnett et al., 1983). Cassini has a dedicated dust instrument on board the Cosmic Dust Analyzer (CDA; Srama et al., 2004), which is designed to measure the size, density, velocity, charge, and composition of the dust particles. The Radio and Plasma Wave Science (RPWS) instrument is also sensitive to dust impacts during the faint ring crossings (Gurnett et al., 2004). During the Cassini mission, the spacecraft crossed the ring plane at various radial distances, providing valuable in situ measurements of dust particles in the Enceladus plume and Saturn's faint rings (Dong et al., 2015; Hill et al., 2012; Kempf et al., 2008, 2010; Kurth et al., 2006; Spahn, Schmidt, et al., 2006; Srama et al., 2006; Wang et al., 2006; Ye, Gurnett, & Kurth, 2016; Ye et al., 2014).

Cassini was in its Ring Grazing orbits between 30 November 2016 and 22 April 2017. At periapsis of these high inclination orbits, the spacecraft crossed the ring plane between the F and G rings at around 2.5 R_S (Saturn radius 60,268 km). The ring plane crossing locations are close to the orbit of the coorbital moons Janus

and Epimetheus. This region is populated with dust particles that belong to the faint Janus-Epimetheus ring. The moons Janus and Epimetheus and the E, F, and G rings are the most likely sources of these particles (Seiß et al., 2017). Based on plasma density data collected during the Saturn orbit insertion and in 2007, Johnson et al. (2017) inferred the density of nanometer-sized particles between the F and G rings. RPWS can provide direct measurement of dust density and size distribution through its Wideband receiver (WBR), and the dust density can also be inferred from differences in electron and ion densities measured by the Langmuir probe around the ring plane crossings (Morooka et al., 2018). During most of the ring plane crossings, the CDA High Rate Detector (HRD) can provide density and size measurements of the dust particles for comparison with RPWS data.

In this paper, we will focus on analyzing the RPWS WBR data collected during the ring plane crossings of the Ring Grazing orbits. First, we will briefly discuss the detection mechanisms. We will show the RPWS data and compare with CDA measurements. Then we will discuss the faint ring structure shown by this data set.

2. Dust Detection With RPWS WBR

The dust detection by wave instruments with electric field antennas is based on impact ionization which converts the impact kinetic energy into electric signals (Aubier et al., 1983; Gurnett et al., 1983; Meyer-Vernet, 1985). The high-speed impact vaporizes the dust particle and part of the spacecraft surface material, which results in a hot ionized gas where electrons and ions are either collected by the target or expelled depending on the spacecraft potential. This charge separation and recollection by the spacecraft body or electric antenna element creates a voltage difference between the antenna elements, which leads to a transient voltage jump signal in the Cassini RPWS receiver WBR (Gurnett et al., 2004). Similar dust impact signals have also been observed by wave instruments on board other spacecraft (Gurnett et al., 1987, 1991; Kellogg et al., 2016; Malaspina et al., 2014; Vaverka et al., 2017; Zaslavsky et al., 2012). Dust properties like size and densities can be computed from the voltage jump size and count rate of the dust impact signals detected by WBR. A description of how RPWS measurements are converted to grain size and density is given by Ye, Gurnett, and Kurth (2016).

The generation of impact signals on the electric field antennas has been simulated with impact experiments, where submicron-sized iron particles were launched at high speed onto a spacecraft model in a vacuum chamber (Collette et al., 2015). More recently, Nouzák et al. (2017) doing the similar experiment with a 1:20 Cassini model as target confirmed that the dipole antenna detects primarily impacts on the antenna elements, whereas the monopole antenna detects impacts on both the antenna and the spacecraft body (including the high-gain antenna, HGA; Ye, Kurth, Hospodarsky, Averkamp, & Gurnett, 2016). The waveforms recorded in the experiment show that the decay time scale of the impact signals varies with the target due to different capacitances of the antenna elements and spacecraft body, and the rise time is longer with positively charged targets, when the ion escaping velocity is slower than electron escaping velocity (Ye, Kurth, Hospodarsky, Averkamp, Gurnett, Sternovsky, et al., 2016). These findings are important to understanding the generation mechanism of the antenna signals and can be used to validate the theoretical works by Zaslavsky (2015) and Meyer-Vernet et al. (2017).

3. Observations

Cassini started its Ring Grazing orbits on 30 November 2016, when it shifted to a high inclination orbit, crossing the ring plane just outside the main rings on the dayside every ~7 days. Both RPWS and CDA detected dust impacts during the ring plane crossings (when CDA was not shielded by the HGA). RPWS WBR had high-resolution (2–4 snapshots per second depending on the bandwidth) data coverage of all the periapsis of the Ring Grazing orbits. The 20 Ring Grazing orbits ended on 22 April 2017, providing valuable in situ measurements near the Janus/Epimetheus orbit.

Figure 1 shows an example RPWS WBR wave power spectrogram, which covers a 1-hr period around the Orbit 254 ring plane crossing on 26 December (day of year, DOY 361) 2016. The antenna mode was switched from dipole to monopole at around 1:19 and switched back to dipole at around 1:48 (UTC). The monopole antenna has a larger detection area and can detect more dust impacts for better characterization of the size distribution (Ye, Kurth, Hospodarsky, Averkamp, & Gurnett, 2016). The monopole antenna was used to measure dust impacts during the ring plane crossing at around 1:32. Note the sharp changes in wave power at the times of antenna switches. Similar differences between the monopole and dipole antennas have also been reported

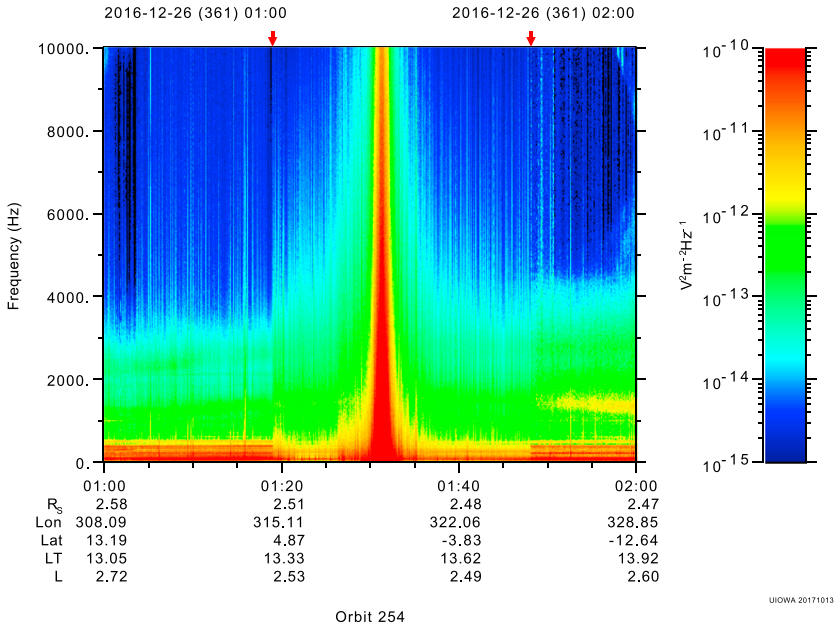

Figure 1. Radio and Plasma Wave Science Wideband receiver electric field power spectrogram, covering 1 hr around the ring plane crossing on day of year 361, 2016. The antenna mode was monopole at the ring plane crossing around 1:32 (UTC). The red arrows at around 1:19 and 1:48 mark the times of antenna mode change, from dipole to monopole and back.

in other spacecraft observations (e.g., Meyer-Vernet et al., 2014; Tsintikidis et al., 1994). The difference in spectral power at the antenna switch could be due to a lower impact rate, a smaller average voltage pulse size, or both, as the spectral power is proportional to the product of impact rate and average squared voltage pulse amplitude (Meyer-Vernet et al., 2009). Ye, Kurth, Hospodarsky, Averkamp, and Gurnett (2016) compared the waveforms recorded using monopole and dipole antennas during a ring plane crossing and showed that the impact signals recorded by the monopole and dipole antennas are similar in size and the monopole antenna recorded a higher impact rate due to the larger effective impact area.

Figure 2 shows the statistics of dust impacts observed during the ring plane crossing on DOY 361, 2016. Figure 2a shows the impact counts as a function of voltage and time. Note the sharp change in dust impact counts as the antenna mode was switched from dipole to monopole and back. Figure 2b shows the gain of the receiver, which is set based on waveform amplitudes to maximize the use of the analog-to-digital converter dynamic range while minimizing clipping (exceeding the range of the analog-to-digital converter; Gurnett et al., 2004). The gain is automatically controlled by onboard software once every few seconds and applied between waveform snapshots. The automatic gain control helps expand the dynamic range of the WBR and its sensitive size range (submicron to 10 μm). The gain decreased as Cassini approached the ring plane, where there were more larger dust particles and the dust impact signals were strongest. With less amplification, impact signals due to smaller particle impacts became unidentifiable, which led to a larger detection size threshold at lower gain. Occasionally, large particle impact signals are also clipped due to the 8-bit dynamic range, especially at high gains. Therefore, the sensitive size range of the instrument is inversely correlated with the gain.

Figure 2c shows the dust number density (1-μm size threshold) calculated from the impact rates, assuming an effective impact area of 1 m^2. The sizes are calculated from the voltage jump sizes based on the charge yield relations measured for the surface materials of the spacecraft, Kapton, BeCu, and HGA paint (Collette et al., 2014; Grün, 1984). Details of the voltage to size conversion and discussions of uncertainty can be found in Ye et al. (2014) and Ye, Gurnett, and Kurth (2016). Since the sensitive size range of RPWS changes with the gain (smaller particles not detectable in the low gains), we scaled the impact rates to a fixed size threshold of 1 μm, assuming the size distribution has the same slope within and outside the sensitive size range. The red line represents a horizontal cut of panel (a) at 0.034 V, the voltage that corresponds to 1-μm dust size. The count rate profile for 1-μm particles has a width of ~600 km.

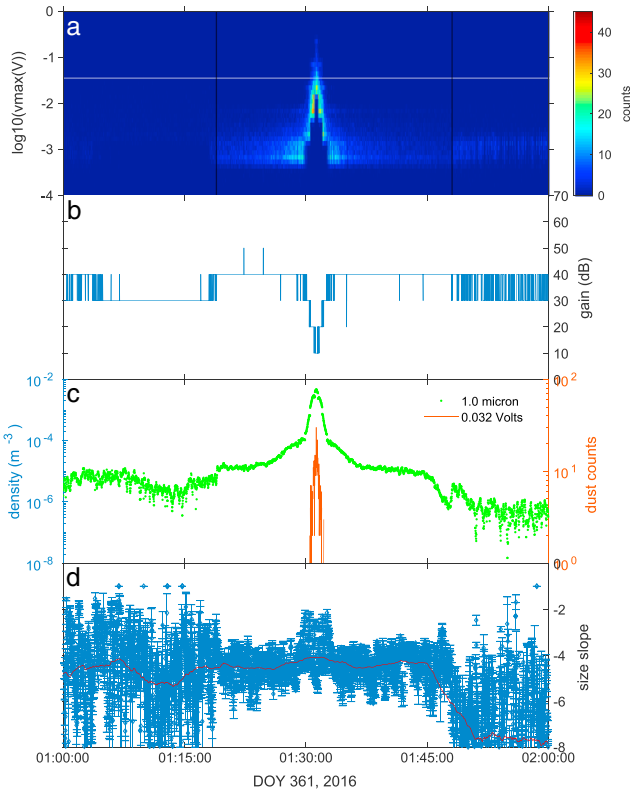

Figure 2. Dust analysis for the ring plane crossing on DOY 361, 2016. (a) Impact counts as a function of voltage and time. Black verticals lines mark the times of the mode changes, between which monopole antenna was used. (b) Gain of the receiver. (c) Dust density (1-μm size threshold) calculated from the impact rates. The red line shows the horizontal cut of panel a at 0.046 V (marked with white horizontal line in panel a). (d) Differential size (radius) distribution slope estimated within a 10-s moving window (blue diamonds, red line shows smoothed value with a 120-s moving window). DOY = day of year.

Figure 2d shows the size distribution slope estimated within a 10-s moving window (blue diamonds). The voltage jump sizes recorded in the moving window are sorted into equal size bins of a histogram. The bin with the most voltage signals is selected as the voltage threshold V_{thd}. Then the number of voltage jumps larger than V_{thd}, $2V_{thd}$, and $4V_{thd}$ are fitted with the associated threshold values. Since particle mass is proportional to the voltage jump size, from the fit we can get the cumulative mass distribution slope $\eta + 1$ (η is the differential mass distribution slope), from which we can derive the differential size distribution slope $\mu = 3\ \eta + 2$ (Ye, Gurnett, & Kurth, 2016; Ye et al., 2014). The scatter of the blue diamonds indicates the uncertainty of the estimated size distribution slope, increased when the number of impacts detected within the moving window decreases. For example, when the antenna mode was switched to dipole, fewer impacts were detected, causing higher uncertainty level of the size slope. The red line indicates smoothed values of the individual size slopes (blue diamonds) using a 120-s moving window. This smoothed size slope is also used to scale the density values to the fixed size threshold shown in Figure 2c.

Figure 3 shows the size distribution histograms for the particles detected during the same ring plane crossing as shown in Figure 2. The particles were separated by the gains they were detected in so that the limited sensitive size range of each gain would not distort the shape of the size distribution histogram. It is shown that within each gain the size distribution exhibits a power law distribution with the lower gains corresponding to higher density levels. The peaks on the right-hand side of the histograms are due to the clipped signals of large particle impacts. The color-coded line segments are power law fits of the size distributions. Note that only the straight power law parts of the histograms (indicated by line extent) were fitted, so the peaks due to the clipped signals were not included. The slopes of the size distributions for different gains range between −4 and −5 (except for 50 dB, where the WBR spent a very short time so the statistics are not as good), consistent with the slopes derived from the threshold fitting method shown in Figure 2d.

4. Results

In Figure 4a, we plot dust density (>1 μm) versus vertical distance from the ring plane for the 20 ring plane crossings of the Ring Grazing orbits. The ephemeris information (1-s resolution) is obtained from the Navigation and Ancillary Information Facility's SPICE kernels (Acton, 1996). The color-coded density profiles are plotted on top of each other with the legend showing the orbit number on the right. It is shown that the shapes of the density profiles are similar to Lorentzian functions with different peak size and width. In Figure 4b, Cassini trajectories during the Ring Grazing orbits are color coded with dust densities (1-μm size threshold) measured by RPWS. The ring plane crossing location shifted between the Janus/Epimetheus orbit and the F ring (2.51 to 2.45 R_S), with the orbits closest to the F ring mainly in the end. It is shown that the dusty ring has a very narrow vertical extent around the ring plane and the measured peak density decreased as the ring plane crossing location moved away from the core of the Janus/Epimetheus ring toward the F ring.

Figure 4c shows a Lorentzian function (red curve) fit of the dust density profile for the ring plane crossing on DOY 361, 2016 (orbit 254). The Lorentzian density model is given by

$$n = \frac{n_0 w^2}{(z - z_0)^2 + w^2} \tag{1}$$

where n_0 is the peak density and z_0 is the vertical offset of the peak density. From this model fitting, the peak density and half width at half maximum (w) of each density profile can be determined. The fitted parameters

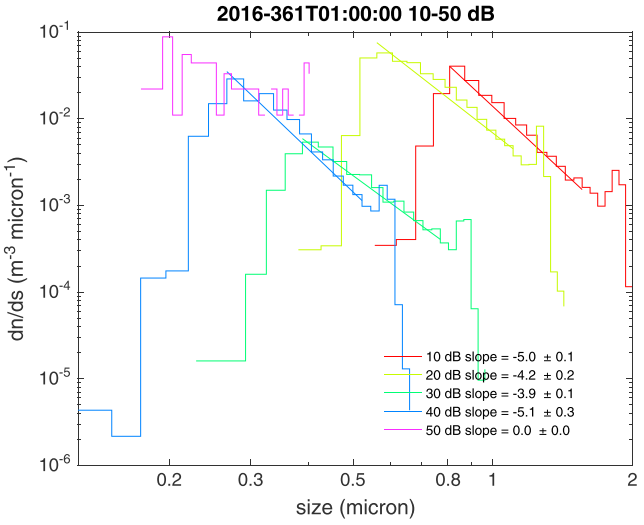

Figure 3. Size distribution histograms for the particles detected during the ring plane crossing on day of year 361, 2016. Particles are separated by the receiver gains in which they were detected. The color-coded lines are power law fits to the size distributions. The size range of the lines indicate the range of the fits.

for the 20 Ring Grazing orbit ring plane crossings are listed in Table 1. The systematic error of these density values was estimated to be around one order of magnitude (Ye et al., 2014), but the shapes of the density profiles and the relative density variations among orbits should not be affected. The vertical thickness (w) of the dusty ring varies between 300 and 500 km, likely controlled by the distance from the Janus/Epimetheus orbit. The peak density (n_0) also varies by 1 order of magnitude (2 to 15 $\times 10^{-3}$ m^{-3}), with the higher densities measured during the early Ring Grazing orbits (December 2016 to March 2017, Orbits 251 to 266), likely because the ring plane crossing locations were closer to the high-density region near the Janus/Epimetheus orbit.

We examined the dependence of Lorentzian fit parameters on factors like radial distance, moon phases, and precession phase (Figure 5). The peak density and width seem to have a weak dependence on radial distance (panels a and b), with higher densities and ring thickness observed close to the Janus/Epimetheus orbit. The density peak location of the dusty ring (z_0) shifts slightly between 100 km south and 100 km north of the ring plane. Panel (c) shows the peak offset z_0 as functions of the phase of the moon Janus (we also tried with Epimetheus phase). The moon phase control is not very clear as the vertical scattering of peak offset values seem to be comparable to the variation with Janus phase. Panel (d) shows the peak offset as a function of precession phase

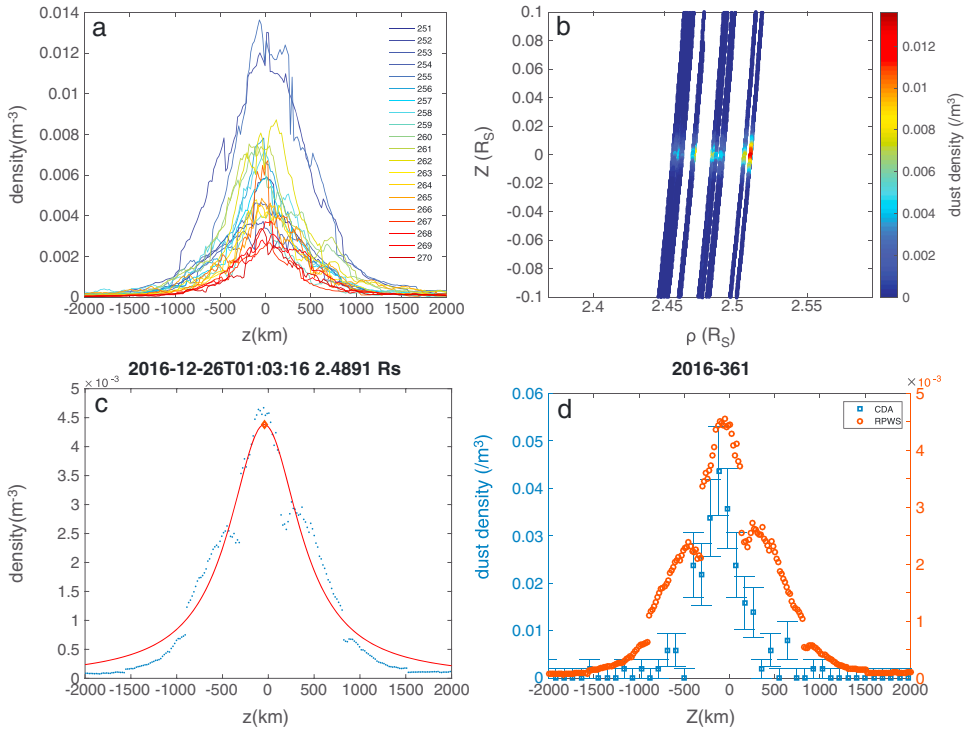

Figure 4. (a) Radio and Plasma Wave Science (RPWS) dust density profiles measured during 20 Ring Grazing orbits. (b) Cassini Ring Grazing orbits trajectories color coded with dust densities (size threshold 1 μm) measured by RPWS. (c) Dust density versus vertical distance from the ring plane, for the ring plane crossing on day of year 361, 2016. The red curve is a Lorentzian function fit of the density profile. The red diamond marks the peak location of the fit. (d) Comparison of vertical dust density profiles measured by RPWS and Cosmic Dust Analyzer High Rate Detector during the ring plane crossing on day of year 361, 2016. There is one order of magnitude difference between the two results, which is within the uncertainty limit estimated for the RPWS measurement (see section 5).

Table 1
Lorentzian Fit Parameters for Vertical Dust Density Profiles of the Ring Plane Crossings During the 20 Ring Grazing Orbits

Time (UTC)	n_0 (m^{-3})	w (km)	z_0 (km)	r_{max} (R_S)
2016-12-4 T13:09:22	0.0053	396	−7	2.5104
2016-12-11 T17:26:03	0.0124	458	4	2.51
2016-12-18 T21:29:34	0.0035	480	−66	2.491
2016-12-26 T01:31:19	0.0042	436	−51	2.4891
2017-1-2 T05:27:06	0.0134	388	45	2.4854
2017-1-9 T09:20:31	0.0072	304	−42	2.4834
2017-1-16 T13:12:16	0.0057	341	−17	2.4844
2017-1-23 T17:05:32	0.0068	352	−13	2.4847
2017-1-30 T21:02:33	0.0041	299	−61	2.486
2017-2-7 T01:25:07	0.0067	436	−76	2.5054
2017-2-14 T05:56:36	0.0076	389	−76	2.506
2017-2-21 T10:02:37	0.0085	338	41	2.4709
2017-2-28 T14:10:20	0.0045	367	6	2.4694
2017-3-7 T18:09:57	0.0046	335	4	2.4597
2017-3-14 T22:05:26	0.0041	431	43	2.4576
2017-3-22 T01:57:25	0.0053	303	11	2.4569
2017-3-29 T05:48:50	0.0025	350	−13	2.4556
2017-4-5 T09:40:16	0.0031	389	76	2.457
2017-4-12 T13:39:51	0.003	344	23	2.4615
2017-4-19 T17:44:27	0.0029	313	19	2.4623

Note. From left to right, the columns of the table are UTC of peak density, peak density for particles larger than 1 μm, half width at half maximum of the Lorentzian fit, vertical offset of the peak location, and radial distance (in *Rs*) of the peak location. The date is formatted as Year-Month-Date.

of the dusty ring, which is computed as the product of the precession rate of Janus (−2.0°/day; Jacobson et al., 2007) and time. The peak offsets seem to be modulated by the precession phase. It appears as though the dusty ring is tilted and precesses as it rotates around Saturn. Since the ring plane crossings took place at around noon local time, Cassini detected different peak offsets as it crossed the ring plane at different precession phases of the dusty ring.

5. Discussion

The RPWS Langmuir probe can indirectly detect the existence of the dust particles via the difference in the measured electron and ion densities (Engelhardt et al., 2015; Morooka et al., 2011; Shafiq et al., 2011; Wahlund et al., 2009; Yaroshenko et al., 2009). The electron depletion is mostly due to absorption by nanoparticles, but with an assumption of the size distribution slope, micron dust density can be inferred, as Morooka et al. (2018) did near the Janus/Epimetheus orbit based on Langmuir probe measurements. The dust density profile is 4–5 times wider than that derived from the RPWS WBR data. This could be due to the fact that Langmuir probe is sensitive to nanoparticles, which can more easily migrate away from the ring plane. Morooka et al. (2018) suggested that the size distribution slope could be steeper away from the ring plane and the micron dust densities derived based on a steeper slope match the WBR micron dust densities outside the narrow peak around the ring plane (their Figure 1). As shown in Figure 2d, WBR observed different values of the dust size distribution slope for the narrow and dense (−4) and the broad and thin (−5) parts of the ring.

CDA made measurements of the Janus/Epimetheus ring when the instrument was not shielded by the HGA. Figure 4d compares the vertical dust density profiles measured by RPWS and CDA HRD during the ring plane

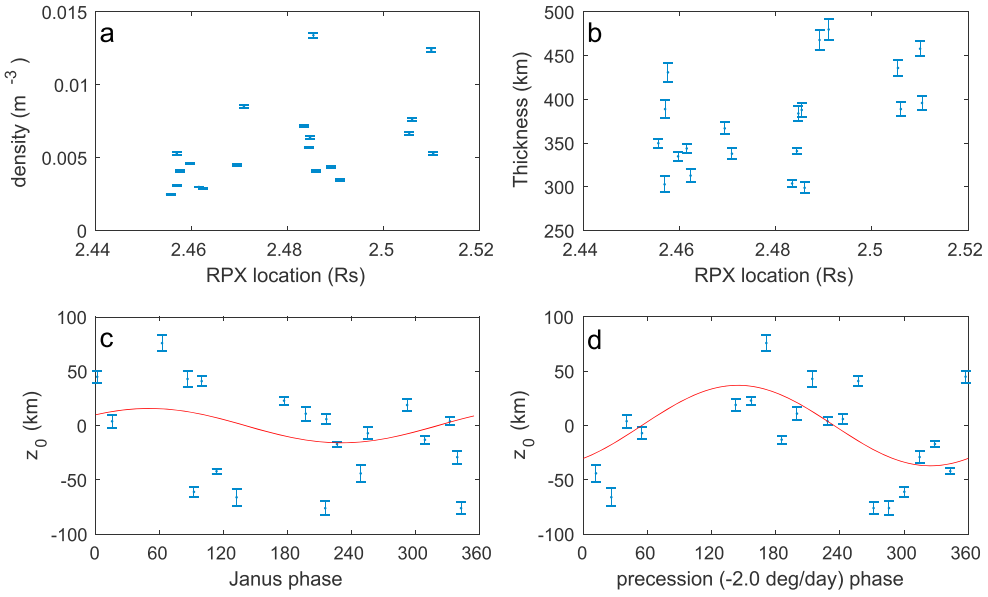

Figure 5. For each of the 20 Ring Grazing orbits, the Radio and Plasma Wave Science dust density profile was fitted with a Lorentzian function. The fitted parameters, peak density, peak vertical offset, and peak width (half width at half height) are listed in Table 1. The parameter values show variation from orbit to orbit. Variation of the Lorentzian fit parameters of the dust density profiles with radial distance, moon phase, and the precession phase of the dusty ring. The red lines in panels (c) and (d) are best sinusoidal fits.

crossing on DOY 361, 2016. HRD uses polarized foils for dust detection and can measure high impact rates of particles bigger than a size threshold that depends on the impact speed (Srama et al., 2004). Discontinuities in the RPWS dust density profile are due to gain changes of WBR. The HRD data showed consistent peak densities around 0.04 m^{-3} (threshold ~ 0.8 μm) during the Ring Grazing orbits, less than 1 order of magnitude higher than the RPWS WBR dust density and within the uncertainty limit of the method (Ye et al., 2014). WBR also measured wider peaks (full width at half maximum, FWHM 600 to 1,000 km) than HRD (averaged profile shows a FWHM of 475 km; Seiß et al., 2017). This could be due to the fact that RPWS is sensitive to different size particles during the ring plane crossing (gain change) whereas HRD is sensitive to a fixed size range of particles. Due to nongravitational forces, the smaller particles that RPWS is sensitive to at higher gains can more easily move away from the plane than the larger grains, so the vertical thickness of the dusty ring is size dependent. During the E ring crossings, the E ring FWHM measured by CDA and RPWS are similar around Enceladus' orbit. But at Mimas' orbit, the width measured by CDA is much smaller than RPWS, and optical measurements are more consistent with RPWS (de Pater et al., 2004; Kempf et al., 2008; Ye, Gurnett, & Kurth, 2016).

The fact that the peak of the Janus/Epimetheus ring has a vertical offset is intriguing. Peak offsets were also observed by the CDA HRD, although no modulation due to the precession was found. Instead, the HRD density profiles on average showed a peak offset of 130 km south of the ring plane (Seiß et al., 2017). Similar offsets have been observed in the density structure of the E ring, which is mainly due to the slow modification of dust orbits by the solar radiation pressure (Hedman et al., 2012; Ye, Gurnett, & Kurth, 2016). The tilt of the E ring is subject to change seasonally when the solar illumination angle changes (Hedman et al., 2012). The orbits of Janus and Epimetheus are slightly inclined by 0.16° and 0.35°, respectively, which result in maximum vertical offsets from the ring plane of 400 km and 1,000 km. Note that the maximum offsets of the moons are greater than the maximum vertical offset of the ring density peak but close to the thickness of the dusty ring measured by CDA and RPWS. The gravity forces from these two moons could play a more important role in tilting and scattering the trajectories of micron-sized dust particles in this ring than nongravitational forces. The coorbital moons of Janus and Epimetheus are locked in horseshoe orbits in a rotating frame, with Janus restricted to a smaller azimuthal angle range (less than 90°). Epimetheus led Janus by about 90° in azimuth during the Ring Grazing orbits. The two moons switch orbits every 4 years, during which the change in relative positions of the two moons could affect the dust dynamics in the dusty ring, thereby causing change in the ring shape. The more massive moon Janus play a more important role in altering the trajectories of dust particles.

6. Summary

We presented the first in situ measurements of the dusty Janus/Epimetheus ring performed during the 20 Ring Grazing orbits of Cassini between December 2016 and April 2017. RPWS WBR data were analyzed to provide density profiles and size distributions of the dust particles in the dusty ring. The RPWS dust density profiles, fitted with Lorentzian functions, are comparable to that measured by the CDA HRD, although the HRD data show slightly higher peak densities and narrower peak widths. The dust densities inferred from the Langmuir probe sweep data (assuming a differential size distribution slope −4.5) agree with the WBR results. The peak locations of the RPWS dust density profiles shift north and south but are within 100 km of the ring plane (CDA HRD density profiles show a systematic southward shift of 130 km). These peak offsets are within the maximum offsets of the moons Janus and Epimetheus due to their slight orbit inclinations, and they seem to be modulated by the precession phase of the Janus/Epimetheus orbit.

Acknowledgments
This research was supported by NASA through contract 1415150 with the Jet Propulsion Laboratory and Deutsches Zentrum für Luft-und Raumfahrt (OH 1401). The data used in this study are available through the Planetary Data System (PDS) or from the authors. We thank Chris Piker and Darrelle Wilkinson for making fast access to the PDS format data possible and Joe Groene and Terry Averkamp for their valuable help with Cassini ephemeris and attitude information.

References

Acton, C. H. (1996). Ancillary data services of NASA's Navigation and Ancillary Information Facility. *Planetary and Space Science*, *44*(1), 65–70.

Aubier, M. G., Meyer-Vernet, N., & Pedersen, B. M. (1983). Shot noise from grain and particle impacts in Saturn's ring plane. *Geophysical Research Letters*, *10*(1), 5–8. https://doi.org/10.1029/GL010i001p00005

Burns, J. A., Hamilton, D. P., & Showalter, M. R. (2001). Dusty rings and circumplanetary dust: Observations and simple physics. In *Interplanetary dust*, (pp. 641–725). Berlin, Heidelberg: Springer. https://doi.org/10.1007/978-3-642-56428-4_13

Collette, A., Grün, E., Malaspina, D., & Sternovsky, Z. (2014). Micrometeoroid impact charge yield for common spacecraft materials. *Journal of Geophysical Research: Space Physics*, *119*, 6019–6026. https://doi.org/10.1002/2014JA020042

Collette, A., Meyer, G., Malaspina, D., & Sternovsky, Z. (2015). Laboratory investigation of antenna signals from dust impacts on spacecraft. *Journal of Geophysical Research: Space Physics*, *120*, 5298–5305. https://doi.org/10.1002/2015JA021198

de Pater, I., Martin, S. C., & Showalter, M. R. (2004). Keck near-infrared observations of Saturn's E and G rings during Earth's ring plane crossing in August 1995. *Icarus*, *172*(2), 446–454. https://doi.org/10.1016/j.icarus.2004.07.012

Dong, Y., Hill, T. W., & Ye, S.-Y. (2015). Characteristics of ice grains in the Enceladus plume from Cassini observations. *Journal of Geophysical Research*, *120*, 915–937. https://doi.org/10.1002/2014JA020288

Engelhardt, I. A. D., Wahlund, J. E., Andrews, D. J., Eriksson, A. I., Ye, S., Kurth, W. S., et al. (2015). Plasma regions, charged dust and field-aligned currents near Enceladus. *Planetary and Space Science*, *117*, 453–469. https://doi.org/10.1016/j.pss.2015.09.010

Grün, E. (1984). Impact ionization from gold, aluminum and PCB-Z. *ESA Special Publications*, *224*, 39–41.

Gurnett, D. A., Grün, E., Gallagher, D., Kurth, W. S., & Scarf, F. L. (1983). Micron-sized particles detected near Saturn by the Voyager plasma wave instrument. *Icarus*, *53*(2), 236–254. https://doi.org/10.1016/0019-1035(83)90145-8

Gurnett, D. A., Kurth, W. S., Granroth, L. J., Allendorf, S. C., & Poynter, R. L. (1991). Micron-sized particles detected near Neptune by the Voyager 2 plasma wave instrument. *Journal of Geophysical Research*, *96*(S01), 19177. https://doi.org/10.1029/91JA01270

Gurnett, D. A., Kurth, W. S., Kirchner, D. L., Hospodarsky, G. B., Averkamp, T. F., Zarka, P., et al. (2004). The Cassini radio and plasma wave science investigation. *Space Science Reviews*, *114*(1-4), 395–463. https://doi.org/10.1007/s11214-004-1434-0

Gurnett, D. A., Kurth, W. S., Scarf, F. L., Burns, J. A., Cuzzi, J. N., & Grün, E. (1987). Micron-sized particle impacts detected near Uranus by the Voyager 2 plasma wave instrument. *Journal of Geophysical Research*, *92*(A13), 14959. https://doi.org/10.1029/JA092iA13p14959

Hamilton, D. P., Skrutskie, M. F., Verbiscer, A. J., & Masci, F. J. (2015). Small particles dominate Saturn/'s Phoebe ring to surprisingly large distances. *Nature*, *522*(7555), 185–187. https://doi.org/10.1038/nature14476

Hedman, M. M., Burns, J. A., Hamilton, D. P., & Showalter, M. R. (2012). The three-dimensional structure of Saturn's E ring. *Icarus*, *217*(1), 322–338. https://doi.org/10.1016/j.icarus.2011.11.006

Hedman, M. M., Burns, J. A., Tiscareno, M. S., Porco, C. C., Jones, G. H., Roussos, E., et al. (2007). The source of Saturn's G ring. *Science*, *317*(5838), 653–656. https://doi.org/10.1126/science.1143964

Hill, T. W., Thomsen, M. F., Tokar, R. L., Coates, A. J., Lewis, G. R., Young, D. T., et al. (2012). Charged nanograins in the Enceladus plume. *Journal of Geophysical Research: Space Physics*, *117*, A05209. https://doi.org/10.1029/2011JA017218

Horányi, M. (1996). Charged dust dynamics in the solar system. *Annual Review of Astronomy and Astrophysics*, *34*(1), 383–418. https://doi.org/10.1146/annurev.astro.34.1.383

Horányi, M., Burns, J. A., Hedman, M. M., Jones, G. H., & Kempf, S. (2009). Diffuse rings. In *Saturn from Cassini-Huygens*, (pp. 511–536). Netherlands: Springer.

Horányi, M., Juhasz, A., & Morfill, G. E. (2008). Large-scale structure of Saturn's E ring. *Geophysical Research Letters*, *35*, L04203. https://doi.org/10.1029/2007GL032726

Jacobson, R. A., Spitale, J., Porco, C. C., Beurle, K., Cooper, N. J., Evans, M. W., & Murray, C. D. (2007). Revised orbits of Saturn's small inner satellites. *The Astronomical Journal*, *135*(1), 261.

Johnson, R. E., Tseng, W. L., Elrod, M. K., & Persoon, A. M. (2017). Nanograin density outside Saturn's A ring. *The Astrophysical Journal Letters*, *834*(1), L6. https://doi.org/10.3847/2041-8213/834/1/L6

Kellogg, P. J., Goetz, K., & Monson, S. J. (2016). Dust impact signals on the wind spacecraft. *Journal of Geophysical Research: Space Physics*, *121*, 966–991. https://doi.org/10.1002/2015JA021124

Kempf, S., Beckmann, U., Klostermeyer, G., Postberg, F., Srama, R., Economou, T., et al. (2008). The E ring in the vicinity of Enceladus I. Spatial distribution and properties of the ring particles. *Icarus*, *193*(2), 420–437. https://doi.org/10.1016/j.icarus.2007.06.027

Kempf, S., Beckmann, U., & Schmidt, J. (2010). How the Enceladus dust plume feeds Saturn's E ring. *Icarus*, *206*(2), 446–457. https://doi.org/10.1016/j.icarus.2009.09.016

Kurth, W. S., Averkamp, T. F., Gurnett, D. A., & Wang, Z. (2006). Cassini RPWS observations of dust in Saturn's E ring. *Planetary and Space Science*, *54*(9-10), 988–998. https://doi.org/10.1016/j.pss.2006.05.011

Malaspina, D. M., Horanyi, M., Zaslavsky, A., Goetz, K., Wilson, L. B., & Kersten, K. (2014). Interplanetary and interstellar dust observed by the wind WAVES electric field instrument. *Geophysical Research Letters*, *41*, 266–272. https://doi.org/10.1002/2013GL058786

Meyer-Vernet, N. (1985). Comet Giacobini-Zinner diagnosis from radio measurements. *Advances in Space Research*, *5*(12), 37–46. https://doi.org/10.1016/0273-1177(85)90065-1

Meyer-Vernet, N., Lecacheux, A., Kaiser, M. L., & Gurnett, D. A. (2009). Detecting nanoparticles at the radio frequencies: Jovian dust stream impacts on Cassini/RPWS. *Geophysical Research Letters*, *36*, L03103. https://doi.org/10.1029/2008GL036752

Meyer-Vernet, N., Moncuquet, M., Issautier, K., & Lecacheux, A. (2014). The importance of monopole antennas for dust observations: Why Wind/WAVES does not detect nanodust. *Geophysical Research Letters*, *41*, 2716–2720. https://doi.org/10.1002/2014GL059988

Meyer-Vernet, N., Moncuquet, M., Issautier, K., & Schippers, P. (2017). Frequency range of dust detection in space with radio and plasma wave receivers: Theory and application to interplanetary nanodust impacts on Cassini. *Journal of Geophysical Research: Space Physics*, *122*, 8–22. https://doi.org/10.1002/2016JA023081

Morooka, M., Wahlund, J.-E., Andrews, D., Persoon, A. M., Ye, S.-Y., Kurth, W. S., et al. (2018). The dusty plasma disk around the Janus/Epimetheus ring. *Journal of Geophysical Research*, *123*. https://doi.org/10.1002/2017JA024917

Morooka, M., Wahlund, J.-E., Eriksson, A. I., Farrell, W. M., Gurnett, D. A., Kurth, W. S., et al. (2011). Dusty plasma in the vicinity of Enceladus. *Journal of Geophysical Research*, *116*, A12221. https://doi.org/10.1029/2011JA017038

Nicholson, P. D., Showalter, M. R., & Dones, L. (1996). Observations of Saturn's ring-plane crossing in August and November. *Science*, *272*(5261), 509–515. https://doi.org/10.1126/science.272.5261.509

Nouzák, L., Hsu, S., Malaspina, D., Thayer, F. M., Ye, S.-Y., Pavlů, J., et al. (2017). Laboratory modeling of dust impact detection by the Cassini spacecraft. *Planetary and Space Science*. https://doi.org/10.1016/j.pss.2017.11.014

Porco, C. C., Helfenstein, P., Thomas, P. C., Ingersoll, A. P., Wisdom, J., West, R., et al. (2006). Cassini observes the active south pole of Enceladus. *Science*, *311*(5766), 1393–1401. https://doi.org/10.1126/science.1123013

Seiß, M., Srama, R., Hoffmann, H., & Spahn, F. (2017). The dust distribution between F and G ring, American Astronomical Society, DPS meeting #49, id. 104.05

Shafiq, M., Wahlund, J.-E., Morooka, M. W., Kurth, W. S., & Farrell, W. M. (2011). Characteristics of the dust-plasma interaction near Enceladus' south pole.. *Planetary and Space Science*, *59*, 17–25.

Showalter, M. R. (1996). Saturn's D ring in the Voyager images. *Icarus*, *124*(2), 677–689. https://doi.org/10.1006/icar.1996.0241

Showalter, M. R., & Cuzzi, J. N. (1993). Seeing ghosts: Photometry of Saturn's G ring. *Icarus*, *103*(1), 124–143. https://doi.org/10.1006/icar.1993.1062

Showalter, M. R., Cuzzi, J. N., & Larson, S. M. (1991). Structure and particle properties of Saturn's E ring. *Icarus*, *94*(2), 451–473. https://doi.org/10.1016/0019-1035(91)90241-K

Spahn, F., Albers, N., Hörning, M., Kempf, S., Krivov, A. V., Makuch, M., & Sremčević, M. (2006). E ring dust sources: Implications from Cassini's dust measurements. *Planetary and Space Science*, *54*(9-10), 1024–1032. https://doi.org/10.1016/j.pss.2006.05.022

Spahn, F., Schmidt, J., Albers, N., Hörning, M., Makuch, M., Seiß, M., et al. (2006). Cassini dust measurements at Enceladus and implications for the origin of the E ring. *Science*, *311*(5766), 1416–1418. https://doi.org/10.1126/science.1121375

Srama, R., Ahrens, T. J., Altobelli, N., Auer, S., Bradley, J. G., Burton, M., et al. (2004). The Cassini Cosmic Dust Analyzer. *Space Science Reviews*, *114*(1-4), 465–518. https://doi.org/10.1007/s11214-004-1435-z

Srama, R., Kempf, S., Moragas-Klostermeyer, G., Helfert, S., Ahrens, T. J., Altobelli, N., et al. (2006). In situ dust measurements in the inner Saturnian system. *Planetary and Space Science*, *54*(9-10), 967–987.

Throop, H. B., & Esposito, L. W. (1998). G ring particle sizes derived from ring plane crossing observations. *Icarus*, *131*(1), 152–166. https://doi.org/10.1006/icar.1997.5851

Tiscareno, M. S. (2013). Planetary rings. In *Planets, stars and stellar systems*, (pp. 309–375). Netherlands: Springer. https://doi.org/10.1007/978-94-007-5606-9_7

Tsintikidis, D., Gurnett, D. A., Granroth, L. J., Allendorf, S. C., & Kurth, W. S. (1994). A revised analysis of micron-sized particle detected near Saturn by the Voyager 2 plasma wave instrument. *Journal of Geophysical Research*, *99*(A2), 2261. https://doi.org/10.1029/93JA02906

Vaverka, J., Pellinen-Wannberg, A., Kero, J., Mann, I., De Spiegeleer, A., Hamrin, M., et al. (2017). Detection of meteoroid hypervelocity impacts on the Cluster spacecraft: First results. *Journal of Geophysical Research: Space Physics*, *122*, 6485–6494. https://doi.org/10.1002/2016JA023755

Wahlund, J. E., André, M., Eriksson, A. I. E., Lundberg, M., Morooka, M. W., Shafiq, M., et al. (2009). Detection of dusty plasma near the E-ring of Saturn. *Planetary and Space Science*, *57*(14-15), 1795–1806. https://doi.org/10.1016/j.pss.2009.03.011

Waite, J. H., Combi, M. R., Ip, W.-H., Cravens, T. E., McNutt, R., Kasprzak, W., et al. (2006). Cassini ion and neutral mass spectrometer: Enceladus plume composition and structure. *Science*, *311*(5766), 1419–1422. https://doi.org/10.1126/science.1121290

Wang, Z., Gurnett, D. A., Averkamp, T. F., Persoon, A. M., & Kurth, W. S. (2006). Characteristics of dust particles detected near Saturn's ring plane. *Planetary and Space Science*, *54*(9-10), 957–966. https://doi.org/10.1016/j.pss.2006.05.015

Williams, G. A., & Murray, C. D. (2011). Stability of co-orbital ring material with applications to the Janus–Epimetheus system. *Icarus*, *212*(1), 275–293. https://doi.org/10.1016/j.icarus.2010.11.038

Yaroshenko, V. V., Ratynskaia, S., Olson, J., Brenning, N., Wahlund, J.-E., Morooka, M., et al. (2009). Characteristics of charged dust inferred from the Cassini RPWS measurements in the vicinity of Enceladus. *Planetary and Space Science*, *57*, 1807–1812. https://doi.org/10.1002/2014JA020024

Ye, S.-Y., Gurnett, D. A., & Kurth, W. S. (2016). In-situ measurements of Saturn's dusty rings based on dust impact signals detected by Cassini RPWS. *Icarus*, *279*, 51–61. https://doi.org/10.1016/j.icarus.2016.05.006

Ye, S.-Y., Gurnett, D. A., Kurth, W. S., Averkamp, T. F., Kempf, S., Hsu, H. W., et al. (2014). Properties of dust particles near Saturn inferred from voltage pulses induced by dust impacts on Cassini spacecraft. *Journal of Geophysical Research: Space Physics*, *119*, 6294–6312. https://doi.org/10.1002/2014JA020024

Ye, S.-Y., Kurth, W. S., Hospodarsky, G. B., Averkamp, T. F., & Gurnett, D. A. (2016). Dust detection in space using the monopole and dipole electric field antennas. *Journal of Geophysical Research: Space Physics*, *121*, 11,964–11,972. https://doi.org/10.1002/2016JA023266

Ye, S.-Y., Kurth, W. S., Hospodarsky, G. B., Averkamp, T. F., Gurnett, D. A., Sternovsky, Z., et al. (2016). Dust impact signals detected by Cassini RPWS: Observations and the laboratory experiments, American Geophysical Union, Fall General Assembly.

Zaslavsky, A. (2015). Floating potential perturbations due to micrometeoroid impacts: Theory and application to S/WAVES data. *Journal of Geophysical Research: Space Physics*, *120*, 855–867. https://doi.org/10.1002/2014JA020635

Zaslavsky, A., Meyer-Vernet, N., Mann, I., Czechowski, A., Issautier, K., Le Chat, G., et al. (2012). Interplanetary dust detection by radio antennas: Mass calibration and fluxes measured by STEREO/WAVES. *Journal of Geophysical Research*, *117*, A05102. https://doi.org/10.1029/2011JA017480